

Thesis Title

A subtitle of your thesis

Author name



Thesis submitted for the degree of
Master in Master's Program Name <change at
main.tex>
60 credits

Department Name <change at main.tex>
Faculty name <change in duoforside.tex>

UNIVERSITY OF OSLO

Spring 2022

Thesis Title

A subtitle of your thesis

Author name

© 2022 Author name

Thesis Title

<http://www.duo.uio.no/>

Printed: Reprosentralen, University of Oslo

Abstract

Contents

1	Introduction	1
I	Theory	3
2	High-Entropy alloys	4
2.1	Fundamentals	4
2.2	Core effects and properties	7
3	Modeling of random alloys	9
3.1	The Special Quasi-random Structure model	9
3.1.1	Mathematical description	10
3.1.2	Applications to high-entropy alloys	12
4	Density Functional Theory	16
4.1	Review of Quantum Mechanics	17
4.1.1	The Shrödinger equation	17
4.1.2	Approximations to the many-body Shrödinger equation	18
4.2	Kohn-Sham density functional theory	20
4.2.1	Density functional theory	20
4.2.2	The Kohn-Sham Equation	21
4.3	Limitations of DFT	22
II	Method	24
5	Practical aspects of DFT	25
5.1	The Exchange-Correlation functional	25
5.1.1	Local density approximation	25
5.1.2	Generalized gradient approximation	26
5.1.3	Meta-GGA	26
5.1.4	Hybrid functionals	27
5.1.5	Outlook	27
5.2	Plane waves and reciprocal space	28
5.3	Self-consistent field calculation	30

6	Computational details	32
6.1	Settings and dependencies	32
6.2	Material	33
III	Results and Discussion	35
7	(CrFeMnNi)Si₂ in the β-FeSi₂ structure	36
7.1	Bulk β -FeSi ₂	36
7.2	(CrFeMnNi)Si ₂ SQSs	37
7.2.1	The band gap	39
7.2.2	Local and projected density of states	42
7.2.3	The band gap with SCAN and HSE06	44
7.2.4	Pair distribution functions	49
7.2.5	SQS size	51
8	Other compositions	55
8.1	Exploring the quaternary phase-diagram	55
8.2	High entropy silicides with cobalt and titanium	59
IV	Conclusion	66
10	Overview and outlook	65
10.1	Literature	65
10.2	General thoughts	66
10.3	Other things	70
10.4	Cr ₄ Fe ₄ Mn ₄ Ni ₄ Si ₃₂ in different crystal structures	73
10.5	Overview	75
A	Compositions	66
A.1	Projected density of states	66
A.2	Probability distribution functions	69
B	Eqvimolar alloy	71
B.1	DOS	71
C	Charge density	80

List of Figures

2.1	Formation of HEA based on δ and N . Figures adopted from [hea2016_ch2]	6
2.2	A schematic illustration of lattice distortion in high-entropy alloys. Figure from [owen_jones_2018]	8
3.1	PDFs of (a) 20 and (b) 250 atom SQS models of CrFeMnNi [hea2016_ch10]	13
3.2	Density of states with SQS and MC/MD of FCC CoCrFeNi, figure from [hea2016_ch10]	14
3.3	Probability distribution functions with SQS and MC/MD of HCP CoOsReRu [hea2016_ch10]	14
4.1	Number of DFT studies per year from 1980 to 2021 [dimensions].	16
5.1	Calculated to experimental band gap measurements of Becke-Johnson, modified Becke-Johnson and SCAN functionals [xc_benchmark]	27
5.2	Self consistent iteration of a DFT calculation. Figure adopted from lecture notes fys-mena4111 [persson2020]	30
6.1	5 distinct 48 atom SQS of $\text{Cr}_4\text{Fe}_4\text{Mn}_4\text{Ni}_4\text{Si}_{32}$ based on the β -FeSi ₂ crystal structure. Illustrated with VESTA [vesta]	33
7.1	Density of states (PBE) β -FeSi ₂	36
7.2	Density of states of SQS D (CrFeMnNi)Si ₂ with PBE.	39
7.3	Density of states of SQS B (CrFeMnNi)Si ₂ with PBE.	39
7.4	Local density of states of Si (SQS D)	42
7.5	Local density of states of (a) Cr, (b) Mn, (c) Fe, (d) Ni in SQS D.	42
7.6	Projected density of states SQS D CFMN (fesi2) from PBE calculation	43
7.7	Projected density of states of SQS D and B around E_F	43
7.8	Density of states illustrating the band gaps from PBE and SCAN calculations for SQS E and D.	45
7.9	Density of states of SQS B with HSE06	45
7.10	Probability distribution function of SQS D (top) and B (bottom)	49
7.11	CPU time	51
7.12	Density of states of SQS E 192 atom SQS.	53

7.13	Pair distribution functions of SQS sizes (top) 48 atoms, (middle) 96 atoms, (bottom) 192 atoms	54
8.1	Projected density of states of (a) $\text{Cr}_3\text{Fe}_3\text{Mn}_7\text{Ni}_3\text{Si}_{32}$ (SQS B), (b) $\text{Cr}_5\text{Fe}_5\text{Mn}_3\text{Ni}_3\text{Si}_{32}$ (SQS C), (c) $\text{Cr}_5\text{Fe}_3\text{Mn}_5\text{Ni}_3\text{Si}_{32}$ (SQS A), (d) $\text{Cr}_3\text{Fe}_5\text{Mn}_5\text{Ni}_3\text{Si}_{32}$ (SQS D)	58
8.2	Projected density of states of $\text{Cr}_3\text{Fe}_3\text{Mn}_3\text{Ni}_7\text{Si}_{32}$ around E_F .	58
8.3	Projected density of states of $(\text{CrFeMnCo})\text{Si}_2$	62
8.4	Density of states of a) $(\text{CrFeCoNi})\text{Si}_2$ and b) $(\text{CrFeTiNi})\text{Si}_2$. .	63
8.5	Density of states of two lesser stable SQSs of $(\text{CoFeMnNi})\text{Si}_2$. .	63
A.1	$\text{chCr}_4\text{Fe}_4\text{Co}_4\text{Ni}_4\text{Si}_{32}$	66
A.2	$\text{chCo}_4\text{Fe}_4\text{Mn}_4\text{Ni}_4\text{Si}_{32}$	67
A.3	$\text{chCr}_4\text{Fe}_4\text{Mn}_4\text{Co}_4\text{Si}_{32}$	67
A.4	$\text{chCr}_4\text{Fe}_4\text{Ti}_4\text{Ni}_4\text{Si}_{32}$	68
A.5	$\text{chCr}_4\text{Fe}_4\text{Mn}_4\text{Ti}_4\text{Si}_{32}$	68
A.6	Probability distribution functions of top: $\text{Co}_4\text{Fe}_4\text{Mn}_4\text{Ni}_4\text{Si}_{32}$ (SQS D), middle: $\text{Cr}_4\text{Fe}_4\text{Co}_4\text{Ni}_4\text{Si}_{32}$ (SQS B), bottom: $\text{Cr}_4\text{Fe}_4\text{Mn}_4\text{Co}_4\text{Si}_{32}$ (SQS B)	69
A.7	Probability distribution function of top: $\text{Cr}_4\text{Fe}_4\text{Mn}_4\text{Ti}_4\text{Si}_{32}$ (SQS B), bottom: $\text{Cr}_4\text{Fe}_4\text{Ti}_4\text{Ni}_4\text{Si}_{32}$ (SQS B))	70
B.1	Density of states SQS A $(\text{CrFeMnNi})\text{Si}_2$ with PBE.	71
B.2	Density of states SQS E $(\text{CrFeMnNi})\text{Si}_2$ with PBE.	72

List of Tables

7.1	Total energy per atom, final magnetic moment and band gap of 5 unique SQS of (CrFeMnNi)Si ₂ based on the β -FeSi ₂ unit cell.	37
7.2	Band gap of the 5 SQSs of (CrFeMnNi)Si ₂ calculated from the eigenvalues in spin up, down and total.	40
7.3	Band gap of SQS D as a function of occupancy in the eigenvalues.	41
7.4	Band gap calculated with PBE, SCAN and HSE06 XC-functionals of (CrFeMnNi)Si ₂ SQSs.	44
7.5	Minimum gap between k-point in valence band and conduction band in SQS B from PBE, SCAN and HSE06	46
7.6	Band gap from HSE06 calculations with gaussian smearing and smearing width <i>sigma</i> equal to 0.05 and 0.005, and the tetrahedron method (TBC). "-" mean unchanged values, "ND" means not done.	47
7.7	Total energy, magnetic moment and formation energy of 48, 96 and 192 atom SQSs of (CrFeMnNi)Si ₂	51
7.8	Band gap of SQSs of 48, 96 and 192 atoms each of (CrFeMnNi)Si ₂ . The names are arbitrary, ie A in 48 does not equal A in 96 or 192.	52
8.1	Summary composition diagram	55
8.2	Band gaps of various compositions of (CrFeMnNi)Si ₂ . Most stable SQS of a set is highlighted in bold text, defect band gap are listed in cursive. Some SQSs were excluded from the table due to unsuccessful calculations.	57
8.3	Overview new compositions	60
8.4	Final magnetic moment of the most stable supercell of each composition.	61
8.5	Band gaps of the most stable SQS of β -FeSi ₂ high-entropy silicide compositions as a function of occupancy in the eigenvalues.	61
10.1	Mean and stadard deviation of the total energy and magnetic moment per atom, plus enthalpy of formation of the listed mean energies (FeSi ₂).	68

10.2 Total and spin dependent band gap of 4 permutations of CFMN (fesi2) with PBE GGA calculation. The structures that are excluded from this list either failed in calculations, or does not show any band gap.<	70
---	----

Preface

Chapter 1

Introduction

some introduction on the importance of discovering new materials and alloying.

Need something on thermoelectricity related to both the band gap and high-entropy alloys.

High-entropy alloys is a novel class of materials based on alloying multiple components, as opposed to the more traditional binary alloys. This results in an unprecedented opportunity for discovery of new materials with a superior degree of tuning for specific properties and applications. Recent research on high-entropy alloys have resulted in materials with exceedingly strong mechanical properties such as strength, corrosion and temperature resistance, etc **find references**. Meanwhile, the functional properties of high-entropy alloys is vastly unexplored. In this study, we attempt to broaden the knowledge of this field, the precise formulation of this thesis would be an exploration on the possibilities of semiconducting high-entropy alloys.

A key motivation of this thesis is the ability to perform such a broad study of complex materials in light of the advances in material informatics and computational methods. In this project, we will employ Ab initio methods backed by density functional theory on top-of the line supercomputers and software. 20 years ago, at the breaking point of these methods, this study would have been significantly narrower and less detailed firstly, but secondly would have totaled ... amount of CPU hours to complete (**Calculate this number**). In the addition to the development in computational power, is also the progress of modeling materials, specifically we will apply a method called Special Quasi-random Structures (SQS) to model high-entropy alloys or generally computationally complex structures. Together with the open landscape of high-entropy alloys described above, these factors produce a relevant study in the direction of applying modern computational methods to progress the research of a novel material class and point to promising directions for future research.

In specifics, this thesis revolve around the electrical properties of high-entropy alloys, mainly the band gap as this is the key indicator for a semiconducting material and it's applicability. Semiconductors are the building blocks in many different applications in today's world, ranging

from optical and electrical devices, to renewable energy sources such as solar and thermoelectricity. Given the economic and sustainable factors concerning silicon, in addition to its role in relevant applications such as microelectronics and solar power. Silicon emerges as a natural selection to build our alloys around. Furthermore, the development and research on both high entropy alloys and metal silicides have been heavily centered around 3d transition metals. Keeping in line with the economic and environmental factors, we will continue this direction by focusing on high entropy stabilized sustainable and economic 3d metal silicides **Not happy with this writing**. Throughout the study we will analyze a great number of permutations of 3d silicides, from different initial metal silicides such as $CrSi_2$, $FeSi_2$, $MnSi_{1.75}$, Fe_2Si , each with distinct properties relating to the band gap, crystal structure and metal to silicon ratio. In addition, the permutations include numerous metal distributions and elements within the 3d-group of metals. Examples are Co, Cr, Fe, Mn, and Ni.

Given a background in high-entropy alloys, one could ask if this study is truly sensible. In the later sections we will cover the details of this field, and it quickly become clear that the materials investigated in this study does not fall under the precise definition of high-entropy alloys, nor do we intend to explore the properties and factors relating to high-entropy stabilized alloys such as the configurational entropy, phase stability and finite temperature studies. However this study is motivated from the discovery of these materials and promising properties, and venture into a more hypothetical space of materials, enabled by the computational methods available to study the potential properties of such materials. On the other hand, very recent studies **Mari, and other HEA silicide study** have experimentally synthesized high-entropy disilicides, thus in some way justifying the direction of this project.

We begin this project by reviewing key concepts of solid-state physics for readers lacking a background in materials science, and an introduction to the base 3d silicides of the experimental work. Later follows a theoretic walk-through of the relevant concepts of this thesis, these topics include high-entropy alloys, special quasi-random structures, and density functional theory. Next we shine light on the implementation of DFT in this project, and other computational details required to reproduce the results in this thesis, such as the use of the Vienna Ab Initio Simulation Package (VASP) and implementation of SQS. Finally we present the results of our study, these include the band gap and electronic properties of various structures and the success and challenges of the computational methods applied throughout the study.

Part I

Theory

Part II

Method

Part III

Results and Discussion

Chapter 7

(CrFeMnNi)Si₂ in the β -FeSi₂ structure

7.1 Bulk β -FeSi₂

β -FeSi₂ is a well known semiconductor with an experimentally measured band gap of around 0.85 eV at room temperature [1]. The nature of the band gap is under debate, all though most ab initio studies point to an indirect gap, experimental work result in a direct gap. In our study we find an indirect band gap of 0.65 eV with PBE, in comparison materials project find a band gap of 0.70 eV. This slight discrepancy is most likely down to use of different parameters in the calculations, for example the cutoff energy or number of k-points. In accordance with materials project we find that this compound is nonmagnetic. This can be seen in the electronic density of states in figure 7.1 by that the DOS and hence band gap is identical in both spins.

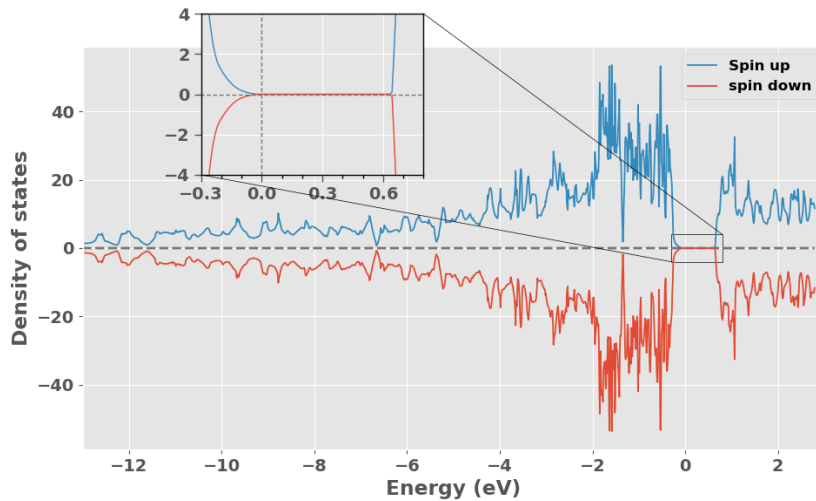


Figure 7.1: Density of states (PBE) β -FeSi₂

The formation energy of the compound can be calculated as the

difference in total energy between the product and the sum of reactants. For the FeSi_2 compound that consist of 16 iron atoms and 32 silicon we get $\Delta H_f = -327.72\text{eV} - (16 \times -8.32\text{eV} + 32 \times -5.42\text{eV}) = -21.16\text{eV}$, or formation energy per atom $E_{FPA} = 0.441\text{eV}$ per atom. The total energy of iron and silicon was calculated separately for the respective base elements with identical parameters as used for the FeSi_2 calculation. Moreover we find that our calculated total energies for both base silicon and iron correspond well with the listed energies from materials project of -5.4234 eV and -8.4693 eV. Accordingly the formation energy per atom of our calculations of 0.441 eV is in agreement with materials project's formation energy of 0.444 eV for β - FeSi_2 . Again, the difference in values is most likely down to materials project utilizing a larger energy cutoff of 520 eV compared to our value of 300 eV.

7.2 (CrFeMnNi)Si₂ SQSs

Below in table 7.1 we list the total energy per atom (Toten), final magnetic moment (Mag) and band gap (E_G) of the five distinct SQSs, plus the formation energy calculated from the mean total energy of the 5 SQSs.

SQS	Toten (eV)	Mag (μ_B)	E_G (eV)
A	-6,6080	0.0833	0.0280
B	-6,6138	0.0833	0.0523
C	-6,6063	0.0834	0.0344
D	-6,6155	0.0833	0
E	-6,6089	0.0833	0.0495
Mean	-6.6105	0.0833	0.0328
Std	0.0039	0.0000	0.0210
$E_{FPA}(\text{eV})$	-0.293	-	-

Table 7.1: Total energy per atom, final magnetic moment and band gap of 5 unique SQS of (CrFeMnNi)Si₂ based on the β - FeSi_2 unit cell.

In addition to the mean energy we include the standard deviation "std" of the set to observe how far each supercell is from the mean value for different properties. Clearly both the total energy and magnetic moment show very little variation if any between SQSs which is expected seeing as the only difference is the atomic configuration. Contrary we observe greater variation in the band gap between SQSs, ranging from 0.02 - 0.05 eV, nevertheless much smaller than the the parent bulk material. On the other side we find that the magnetic moment has increased compared to in the bulk structure. Seen throughout all SQSs, the local magnetic moments is the largest for Cr followed by Mn, on the other hand the ferromagnetic elements Fe and Ni have small negative moments. This is an odd result, in calculations with identical parameters of the base

elements we find that Cr is non, Fe and ni is .., same with manganese. In HEAs specifically we saw in section 2.2 that in several cases particularly chromium reduce the magnetization of the compound. There are however several uncertainties concerning the listed magnetic values in this project, and the reported values are meant to be superficial indications of the magnetism in the real material. For example we have the limitations mentioned previously about both DFT and special quasi-random structures to model magnetic and particularly paramagnetic materials. The latter especially is as an important factor, as the outcome of the base elements are in much better agreement with other experimental data, such as materials project. This could be related to the SQSs distinct for this project, where we kept the Si sites in the lattice constant and restricted the 3d elements to occupy exclusively the Fe sites in the lattice. Such restrictions could impact the magnetic interactions between elements compared to in a real random alloy. Lastly each SQS have been tested solely with co-linear spin polarization, thus neglecting the many other possible configurations. The precise magnetic properties was compromised due to the large computational demand of locating the optimal magnetic configuration of each SQS and composition, and the focus of this project leaning more towards the band gap of the structures more so than the stability and magnetism.

In terms of the total energy the most and least stable SQSs are "D" and "A" respectively. Based on the total energy between SQSs, D is then the most representative configuration of the real material. However most likely all five SQSs and other possible SQSs would appear as local orderings in domains of the real material with a certain probability. Therefore we will consider the results of the other SQSs as well as the most stable supercell. Furthermore the total energy alone is not sufficient to evaluate the stability. In this project we have not considered factors such as the configurational entropy or the optimized magnetic configuration of each structure. Additionally we have only studied the ground state and thus have no knowledge of the properties at finite temperatures. Hence the relationships and properties between the five SQSs listed in table 7.1 are not rigid.

As seen from table 7.1, the enthalpy of formation of this compound far exceeds that of the parent bulk compound. In this case we have no experimental value to measure our results to, but note that the individual energies correspond well with materials project, despite of potential differences in computational settings and methods.

7.2.1 The band gap

The band gap of the alloys are severely reduced from the bulk material, and show variation between each of the five SQSs. We observed a maximum band gap of 0.05 eV in SQS B, and on the flip side a 0 band gap in SQS D. The density of states of SQS D and B is displayed in figures 7.2 and 7.3, DOS plots of the other SQS can be found in appendix .. .

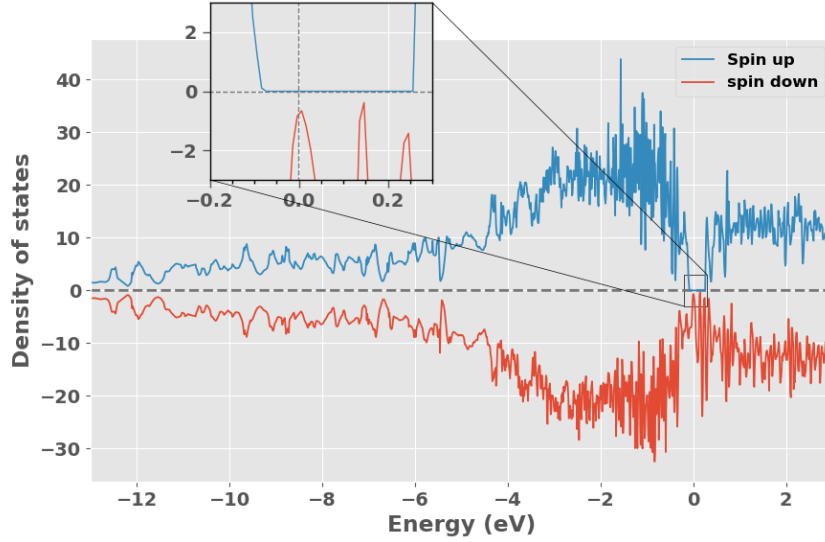


Figure 7.2: Density of states of SQS D (CrFeMnNi)Si₂ with PBE.

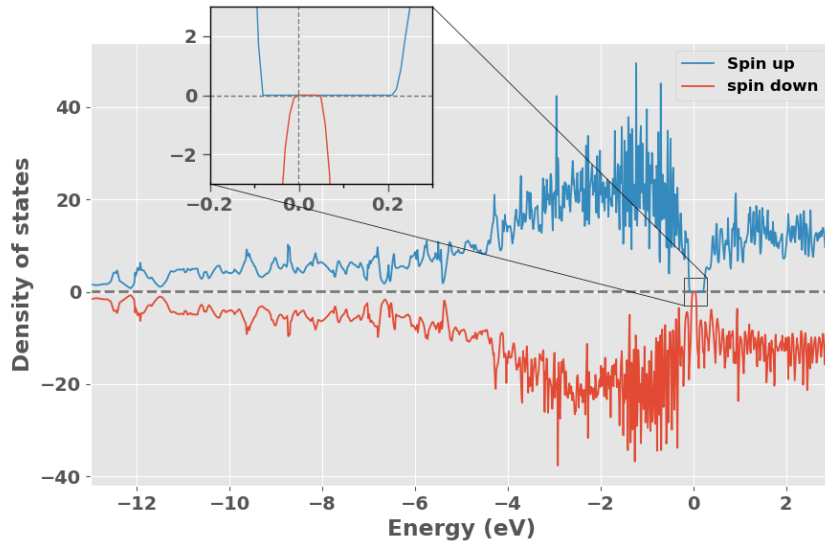


Figure 7.3: Density of states of SQS B (CrFeMnNi)Si₂ with PBE.

In figure 7.2 and 7.3 we observe that the band gap in both SQS D and B in accordance with the magnetic property is different between spins. Going

forward we will refer to the band gap in spin up as E_G^{up} , and spin down as E_G^{dw} . Clearly in both D and B $E_G^{\text{up}} > E_G^{\text{dw}}$ with no gap in spin down in D and 0.05 eV in B compared to around 0.3 eV in spin up in both structures. Comparing to the values listed in table 7.1 it's clear that the total band gaps of the respective structures is limited by the narrow or nonexistent band gap in spin down. To obtain further and more precise information on the band gap we look to the calculated Kohn-Sham eigenvalues. The eigenvalue band gaps, denoted as E_G^{eigen} can be seen below in table 7.2 for all five SQS.

SQS	$E_G^{\text{up, eigen}}$ (meV)	$E_G^{\text{dw, eigen}}$ (meV)	$E_G^{\text{tot, eigen}}$ (meV)
A	81.4	52.2	28.1
B	293	52.2	52.2
C	236	34.3	34.3
D	339	0.00	0.00
E	308	50.0	50.0

Table 7.2: Band gap of the 5 SQSs of (CrFeMnNi)Si₂ calculated from the eigenvalues in spin up, down and total.

We observe a continuing trend across all five SQS similar to D and B where the band gap is limited by the spin down channel, as all SQSs par A display much greater values in spin up. In VASP the energy eigenvalues are listed for every energy band at all k-points used in the calculation, with corresponding occupancy. An occupancy of 1 represents a fully occupied eigenstate, in analog an empty eigenstate have occupancy equal to 0. Recalling that occupied states belong to the valence band, and the conduction band consists of unoccupied states. The highest energy valence band in these SQSs is band 124 in spin down and 128 in spin up, following the lowest energy valence band is 125/129 in spin down/up. The band gap in spin down is then determined from the difference between the lowest energy eigenvalue in band 125 and the highest energy eigenvalue in band 124, and likewise for the spin up band gap between bands 128 and 129. In SQS D different from the semiconducting structures we observe some partially occupied states at the band edges in bands 124 and 125 in spin down. With partially occupied states we refer to eigenstates in the valence band with occupancy less than 1 and states in the conduction band with occupancy above 0. Specifically the highest energy eigenvalue (9.01 eV) in band 124 have occupancy equal to 0.94, and equivalently the lowest eigenvalue (8.98 eV) in band 125 have occupancy equal to 0.08 in this structure (spin down). As seen from the respective energies this results in a 0 (negative) band gap. The fermi energy in this structure is 8.99 eV, the occupied eigenstate in band 124 is then above the fermi energy, and the unoccupied eigenstate in the conduction band is below the fermi energy.

In this project we will refer to such eigenstates with partial occupancy as defect states. The affect of defect states on the band gap of SQS D can

be seen in table 7.3. Here we calculate the band gap as a function of the defect states by an occupancy parameter occ , such that $E_G(0.99, 0.01)$ is the band gap when only including eigenvalues with corresponding occupancy above 0.99 in the valence band and below 0.01 in the conduction band. For simplicity we will write the parameter as a single value, where $occ = 0.1$ represents occupancy equal to $1 - 0.1$ in the valence band and $0 + 0.1$ in the conduction band.

occ	$E_G^{\text{up, eigen}}$ (meV)	$E_G^{\text{dw, eigen}}$ (meV)	$E_G^{\text{tot, eigen}}$ (meV)
0.5	339	0	0
0.05	339	21.0	21.0
0.01	339	49.6	49.6
0.001	339	73.3	73.3
<0.0001	339	85.7	85.7

Table 7.3: Band gap of SQS D as a function of occupancy in the eigenvalues.

The defect states in SQS D is clearly responsible for the 0 spin down band gap, compared to the semiconducting SQSs that only contain fully occupied and empty eigenstates. We relate this concept to a metallic character, as known in a metal the conduction band and valence band overlap. This can be seen in the eigenvalues of a pure metal such as iron, here we calculate the Fermi energy as 5.8. In both spin channels the energy bands around E_F is mostly partially filled eigenvalues, with examples of both more than half-filled states above E_F and less than half-filled states above E_F within the same energy band, thus overlap between the conduction and valence band. Furthermore in a pure semiconductor such as Si we find no partially filled eigenstates as in the semiconducting SQSs. We denote the partially filled states in SQS as defect states rather than simply stating that it's a metal from the fact that the number of such states are very dampend compared to the metal. In SQS D the majority of eigenstates are fully occupied or empty, with some few cases where the occupancy is slightly away from 1 or 0. This have been attributed to a key feature of random alloys [2], but within the scope of this project we are not able to investigate the reason behind it.

It would have been instructive to visualize and analyze the energy bands by plotting the band structure. Unfortunately this is neither simple to perform or interpret in large supercells consisting of several elements and a large number of energy bands. One solution to this is to perform band-unfolding, but this did not work in conjunction with the TDEP implementation of the special quasi-random structures method.

7.2.2 Local and projected density of states

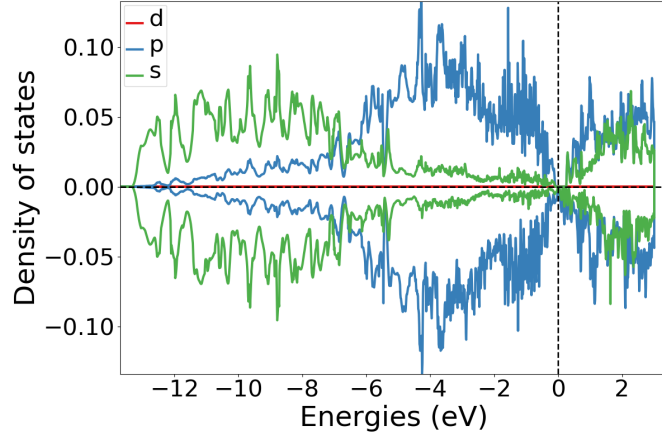


Figure 7.4: Local density of states of Si (SQS D)

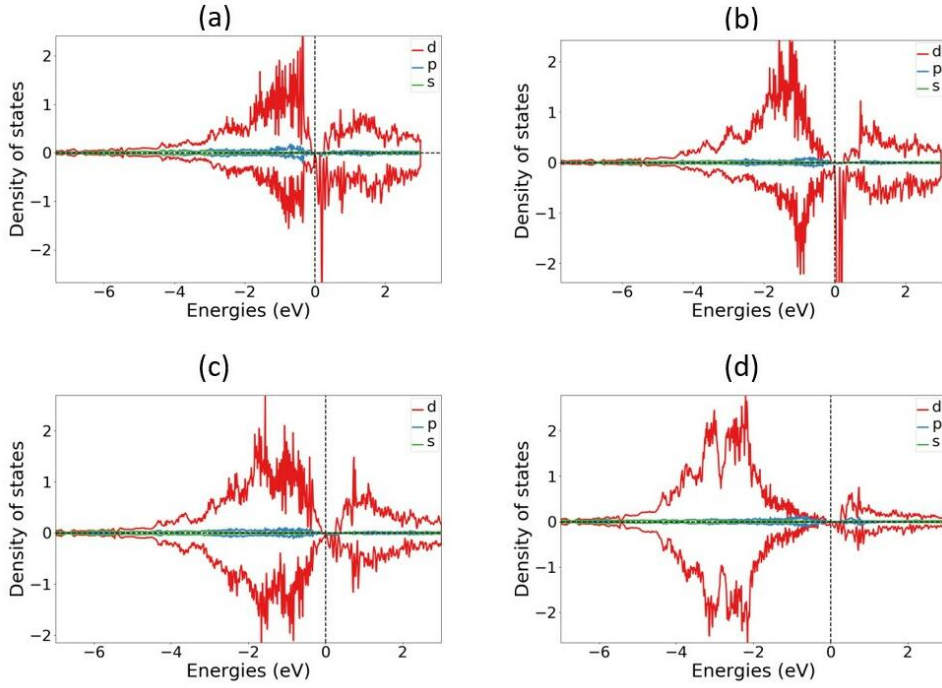


Figure 7.5: Local density of states of (a) Cr, (b) Mn, (c) Fe, (d) Ni in SQS D.

In the local density of states plotted in figure 7.3 we see that the s-electrons in Si occupy states in the lower energy regions and p electrons at slightly elevated energies closer to the Fermi energy, above E_F states are occupied by both s and p electrons almost equally. Further, the local density of states of the transition metals chromium, manganese, iron and nickel in SQS D is displayed bellow in figure 7.4. In spin down, manganese is most dominant especially above E_F , but also bellow E_F . Likewise chromium show a strong

presence above the Fermi energy in spin down. Both iron and Nickel show largest contribution at energies further from the Fermi energy, most notably below E_F . In the spin up channel we see a similar trend where chromium lies closest to E_F followed by manganese then iron and lastly nickel at the lowest energies. Another interesting observation is that the LDOS of iron and nickel is much more symmetric between spins, than Cr and Mn. Comparing to the LDOS of iron and silicon in bulk β -FeSi₂ [3] we find good agreement for both Fe and Si in this alloy.

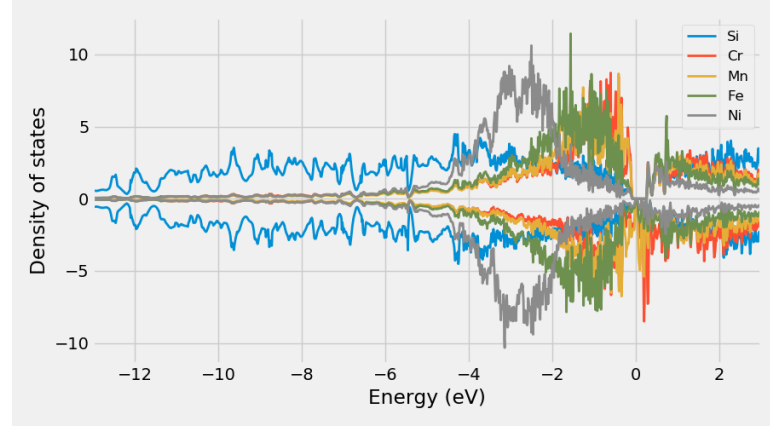


Figure 7.6: Projected density of states SQS D CFMN (fesi2) from PBE calculation

Moreover the relative positions and interplay between 3d elements and silicon as shown in the projected density of states (figure 7.5) is in good agreement with observed trends in simpler Si-rich transition metal silicides [4]. The electronic structure tends to be dominated by TM d electrons, and the valence band density of states are filled by non-bonding d states near E_F . The p-d hybridization between Si and TM elements typically falls about 6 eV below E_F and Si s states about 10 eV below. In our case we find that the Si states are pushed up closer to the Fermi energy by random alloying of various 3d elements.

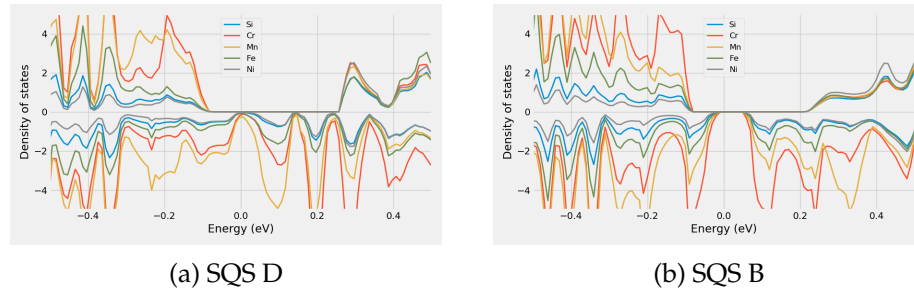


Figure 7.7: Projected density of states of SQS D and B around E_F

Above we have included the PDOS of SQS D and B but focused around E_F , from these figures we find that the spin down channel in D contains a more dominant presence of manganese especially, and some chromium as

compared to the semiconducting SQS B.

7.2.3 The band gap with SCAN and HSE06

As expressed previously in this work we invoke 3 level of depths GGA (PBE), meta-GGA (SCAN) and hybrid functional (HSE06) to determine the band gap of the SQSs, these results are showcased in table 7.4. Note that we do not specify eigen/dos or the occupancy here, because par SQS D the eigenvalues does not contain defect states, hence $E_G^{\text{eigen}}(0.5) = E_G^{\text{dos}}$.

SQS	XC-functional	E_G^{up} (eV)	E_G^{dw} (eV)	E_G^{tot} (eV)
A	PBE	0.0815	0.0521	0.0281
	SCAN	0	0	0
	HSE06	0.7084	0.0261	0.0261
B	PBE	0.2932	0.0523	0.0523
	SCAN	0.1470	0.0890	0.0890
	HSE06	0.2855	0.1819	0.1819
C	PBE	0.2355	0.0343	0.0343
	SCAN	0.0690	0.1124	0.1124
	HSE06	0.1744	0.0328	0.0196
D	PBE	0.3386	0	0
	SCAN	0	0.1086	0
	HSE06	0.3780	0	0
E	PBE	0.3078	0.0495	0.0495
	SCAN	0.1540	0.1112	0.1048
	HSE06	0.5476	0.0133	0.0133

Table 7.4: Band gap calculated with PBE, SCAN and HSE06 XC-functionals of (CrFeMnNi)Si₂ SQSs.

We will begin dissecting table 7.4 by comparing SCAN to PBE. The first distinction we make notice of is in SQS A. In this supercell calculations with the SCAN functional predicts a metallic compound, contrary to the the PBE band gap of 0.03 eV. Alike the band gap of SQS D discussed previously, the 0 band gap in this structure with SCAN is caused by defect states. Neglecting such states and evaluating the band gap from just completely filled and empty eigenstates yield $E_{G,\text{SCAN}}^{\text{up,eigen}}(0.99,0.01) = 0.0316$ eV and $E_{G,\text{SCAN}}^{\text{dw,eigen}}(0.99,0.01) = 0.0531$ eV, and a resulting semiconductor with a band gao of 0.0316 eV. This value seems to agree better with the PBE band gap of this supercell, but we observe that E_G^{up} is larger in PBE. This is a recurrent patter with SCAN across all five SQSs, where $E_{G,\text{SCAN}}^{\text{up}} < E_{G,\text{PBE}}^{\text{up}}$, and moreover $E_{G,\text{SCAN}}^{\text{dw}} > E_{G,\text{PBE}}^{\text{dw}}$. This can be seen in figure 7.7, where we plot the density of states of SQS E (a, b) and C (c, d). Note that the SCAN

band gap in C have the opposite spin polarization compared to PBE, this is also the case in SQS D.

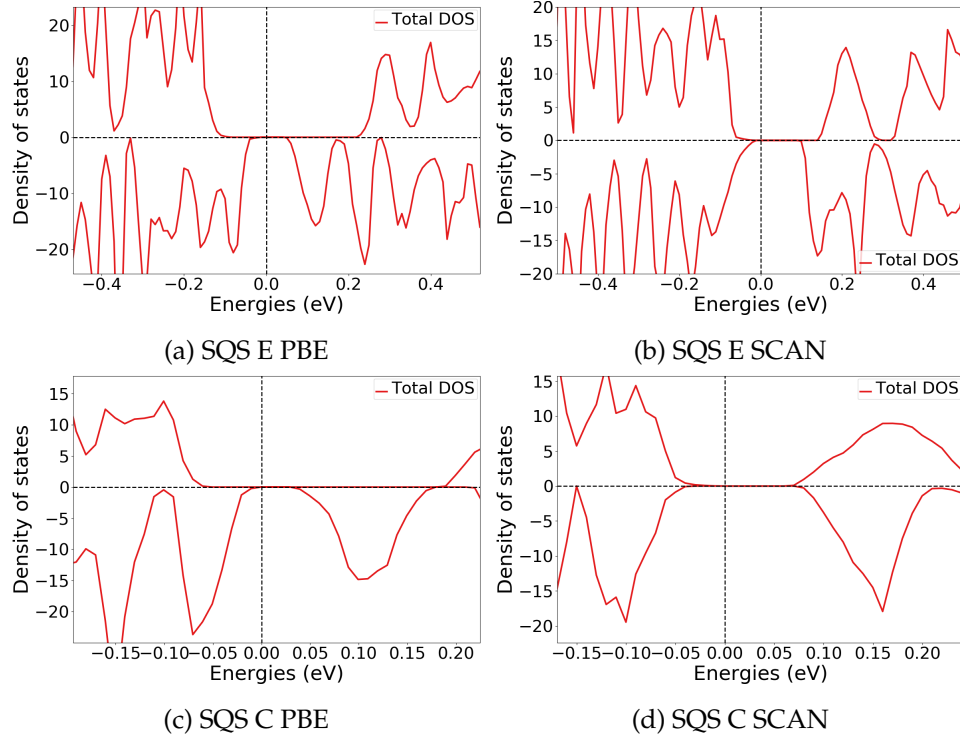
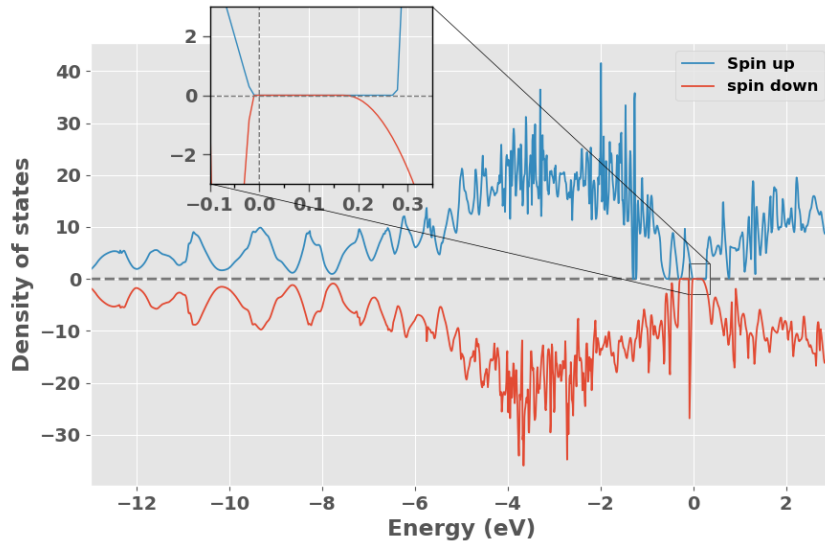


Figure 7.8: Density of states illustrating the band gaps from PBE and SCAN calculations for SQS E and D.



With the HSE06 functional we observe the opposite trend in SQS A and E, where $E_{G, \text{HSE06}}^{\text{up}} > E_{G, \text{PBE}}^{\text{up}}$ and $E_{G, \text{HSE06}}^{\text{dw}} < E_{G, \text{PBE}}^{\text{dw}}$. But in other cases

$E_{G, \text{HSE06}}^{\text{up}}$ is lesser (SQS C) or similar to PBE (SQS B and D). On the other hand $E_{G, \text{HSE06}}^{\text{dw}}$ is consistently smaller in all structures compared to PBE, with the exception of SQS B. In this structure the HSE06 functional predicts large band gaps in both spins, as seen from the density of states plotted in figure 7.8.

As we covered in section 5.1, the hybrid functional is much more computationally demanding compared to SCAN and PBE. To reduce the cost of the HSE06 functional we performed such calculations in this project with a lower density of k-points, see section 6.1. The narrow mesh of k-points is an important factor to mention in relation to the HSE06 band gaps, that could lead to artificially exaggerated band gaps as the low density of k-points could fail to encapsulate the exact minimum transition between the valence band and conduction band.

XC-functional	Transition (k-point)
PBE	(0.250,0.000,0.250) \rightarrow (0.000,0.000,0.000)
SCAN	(0.250,0.000,0.250) \rightarrow (0.000,0.333,0.000)
HSE06	(0.500,0.000,0.000) \rightarrow (0.000,0.000,0.000)

Table 7.5: Minimum gap between k-point in valence band and conduction band in SQS B from PBE, SCAN and HSE06

From table 7.5, we observe that all 3 functionals find different band gaps, a concerning factor is that the highest energy k-point in the valence band from PBE calculations (0.250, 0.000, 0.250) is not considered in the HSE06 calculation with the narrow grid of 2x2x2 k-points. Thus one may suspect that the HSE06 calculation overlook the minimum transition and hence return an enlarged band gap. This could for instance be the case in $E_{G, A}^{\text{up}}$ and $E_{G, B}^{\text{dw}}$ where HSE06 predicts much larger values compared to PBE. However without an experimental baseline of the structure, we can not conclude that this is the case. As in the other SQSs we find examples where HSE06 produce similar or lower values than PBE despite of the smaller number of k-points. The concept of sufficient k-points is especially an important matter in metallic systems, as these are known to require a more dense mesh of points to accurately map the Fermi-surface [5]. However, further investigation of the importance of k-points was not possible within the time-frame of this project.

As stated in section 6.2, we did not manage to converge hybrid calculations with the tetrahedron method, and overcame this problem by first calculating the charge density with Gaussian smearing and utilize the density to expedite calculation with TBC. The respective band gaps from these methods are displayed in table 7.6 for the five SQSs of the (CrFeMnNi)Si₂ system. Here we calculate the band gap from the eigenvalues at different cutoff occupancy *occ* to highlight the part of defect states. Calculations with Gaussian smearing was tested with smearing width *sigma* equal to 0.05 eV and 0.005 eV.

SQS	Smearing (type) width (eV)	$E_G^{up,eigen}$ (0.5) (eV)	$E_G^{dw,eigen}$ (0.5) (eV)	$E_G^{up,eigen}$ (0.99) (eV)	$E_G^{dw,eigen}$ (0.01) (eV)	$E_G^{tot,eigen}$ (0.5) (eV)	$E_G^{tot,eigen}$ (0.99, 0.01) (eV)
A	Gaussian (0.05)	0.7837	0.1493	-	0.2984	0.1493	0.2984
	Gaussian (0.005)	0.2117	0.1013	-	-	0.1013	-
	TBC	0.7084	0.0261	-	-	0.0261	-
B	Gaussian (0.05)	0.2783	0.1702	0.2988	0.3136	0.1506	0.2979
	Gaussian (0.005)	0.2838	0.1823	-	-	0.1801	-
	TBC	0.2855	0.1819	-	-	0.1807	-
C	Gaussian (0.05)	0.1078	0.1066	0.2405	0.1839	0.0650	0.1839
	Gaussian (0.005)	0.1304	0.0222	-	-	0.0222	-
	TBC	0.1744	0.0328	-	-	0.0196	-
D	Gaussian (0.05)	0.3661	0.0592	-	0.1872	0.0592	0.1872
	Gaussian (0.005)	ND	ND	ND	ND	ND	ND
	TBC	0.3780	0	-	0.2665	0	0.2637
E	Gaussian (0.05)	0.6653	0.1439	-	0.1675	0.1439	0.1675
	Gaussian (0.005)	0.5825	0.1211	-	-	0.1211	-
	TBC	0.5476	0.0133	-	-	0.0133	-

Table 7.6: Band gap from HSE06 calculations with gaussian smearing and smearing width σ equal to 0.05 and 0.005, and the tetrahedron method (TBC). "-" mean unchanged values, "ND" means not done.

From table 7.6 we observe that the case of defect states is only a concern at larger smearing widths with Gaussian smearing. Contrary to previous cases, we find here finite band gaps despite of defect states. By comparing E_G^{up} and E_G^{dw} at $\text{occ} = 0.5$ and $\text{occ} = 0.01$, the defects appear to have a lesser role in spin up, as par SQS C the band gap in spin up is either consistent or only marginally different between the defect band gap and the hypothetical defect less band gap. E_G^{dw} on the other hand increase significantly by removing the defect states. The Gaussian smearing method is generally in better agreement with TBC at lower smearing width. But even in this case we find several dissimilarities. In A and E E_G^{dw} is larger with the Gaussian method, additionally E_G^{up} is much lower in A. In this project we have based our choice of numerical smearing on the advice on the VASP manual that state that for accurate total energies and density of states in semiconductors one should opt for the tetrahedron method [6]. However since our system is comprised of metals we include the results from utilizing Gaussian smearing as well. There are of course many more factors that affect the accuracy and reliability of both methods, but these are outside the scope of this project.

The fact that all 3 functionals and five SQS in majority agree on the presence of a band gap is in itself an overwhelmingly positive result that allow us to state with high certainty that the potential high-entropy silicide (CrFeMnNi)Si₂ is in fact a semiconductor or possibly a half-metal based on the observed spin polarization and the utmost stable SQS. Regarding the 3 functionals applied in this project, we experience best cohesion between PBE and HSE06 that both agree on a spin up polarization of the band gap, while SCAN predicts more symmetric band gaps. This can also be seen from the magnetic moment, with PBE and HSE06 the final magnetic moment (per atom) is $0.083 \mu_B$ across all SQSs, with SCAN this is reduced to half as much. This result could be related to the known drawbacks of SCAN and magnetic materials. In the nonmagnetic β -FeSi₂ structure we find better agreement between PBE and SCAN. Both correctly predict that the material is nonmagnetic, however compared to the experimental value of about 0.85 eV and the PBE band gap of 0.65 eV, we get a smaller band gap of 0.61 eV with SCAN. Thus the SCAN functional does not necessarily result in increased accuracy over PBE even in the nonmagnetic material. To conclude this section on the band gap (CrFeMnNi)Si₂, when studying the band gap with DFT, particularly PBE is well known to underestimate the band gap of the real material as in FeSi₂. Therefore a band gap found with PBE would with high probability be replicated/increased in the real material.

7.2.4 Pair distribution functions

The probability distribution functions of SQS D and E can be seen bellow in figure 7.10, the PDFs corresponding to the remaining SQSs can be found in appendix .. . We include the PDFs of SQS D and B because as stated D is the most stable atomic configuration and hence the most representative of a potential real compound, and B to investigate distinctions between the half-metallic structure D and the semiconducting B which with HSE06 yielded substantial band gaps in both spins, recalling also that this is just very slightly bellow D in terms of stability. In the analysis we will put special emphasis on the nearest neighbor interactions since these are the most crucial in deciding the functional properties of a material.

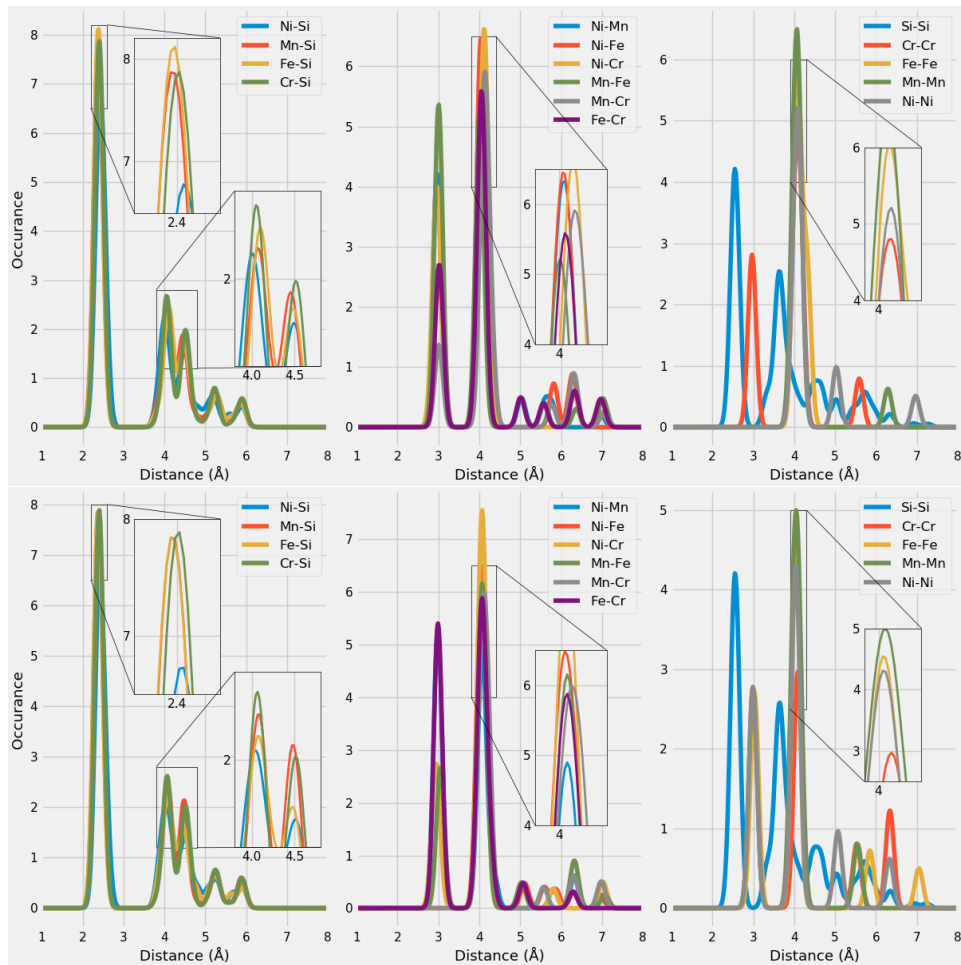


Figure 7.10: Probability distribution function of SQS D (top) and B (bottom)

We see that the relative positions of the PDFs remain consistent though both SQSs. With the aid of the ICSD (insert citation), we can compare the figure .. to the expected PDFs based on a number of experiments from a host of different compounds. As our compound contain a total of 15 different bonds, comparing each one to the ICSD values would be an exhaustive process. For our purpose we are satisfied by comparing the 4

different metal-Si bonds. We find that the preferred bond-length of TM-Si is observed at two values, the most dominant being the shorter of the two. For Fe-Si these are between 2.25-2.75 and 4-5, Mn-Si 2.25-2.75 and 3.5-5. Ni-Si lie between 2.25-2.5 and 3.85-5 and Cr-Si between 2.35-2.65 and 4-5. Clearly, the PDFs of the alloys are in good agreement with the listed values for Tm-Si bonds, with the most occurring bond length falling at around 2.4 Å for all TMs, and lesser occurrence between 4.0 - 4.5 Å. The height of the respective peaks is somewhat consistent in both structures, other than slightly reduced Fe-Si occurrence at 2.4 Å in B.

In contrast to the TM-Si bonds, we observe several distinctions between metal bonds in SQS D and B. Covering all would be tedious and not to insightful, instead we emphasize the bonds of Mn and Cr as this is where we found the biggest discrepancy in the PDOS. From the different TM-TM bonds (middle) of figure 8.8 we observe that the Mn-Fe bonds are most occurring at short distances in D and bigger distances in B, meaning that manganese and iron atoms are placed further from each other in structure D. **correct?** Similarly the bonds between Cr and Fe indicate that these atoms lie closer in B than D. In contrast the nickel and manganese/chromium bonds point to a closer distance in B for Ni-Mn and Ni-Cr in D, and a greater distance between Ni and Mn in D and Ni and Cr in B. **Litt kronglete kanskje?** In terms of the homogeneous bonds, the properties of both Cr-Cr bonds and Mn-Mn bonds are more or less alike in both structures besides some majority at shorter distance in D (The red Cr-Cr line at 3 Å is underneath the grey Ni-Ni line in B in figure 8.8 (bottom right)). A more significant distinction is that both Ni-Ni and Fe-Fe bonds are found at 3 Å and 4 Å in B, but exclusively 4 Å in D.

Both the Fe-Fe and Ni-Ni bonds are in better agreement with the ICSD histograms, as the most occurring distance for these bonds are between 4-4.9 Å and additionally around 2.5 Å. **More comparisons to ICSD, ask O.M.** As a conclusion on the PDFs of this compound, we locate a pattern where the Si-Si bonds are identical and only very minor differences between TM-Si bonds in SQS D and B. This is a result of how the structures are generated with the SQS method. In the FeSi₂ structure the silicon atoms are placed as before in the new supercells, but the TM elements are "randomly" distributed. Thus, it's reasonable that also here we would find the major differences between SQSs in the PDFs.

7.2.5 SQS size

Above we have presented the results of a high-entropy silicide (CrFeMnNi)Si₂ investigated by 5 48 atom SQSs with a volume of 700Å³. This intermediate size allowed for the use of more complex XC-functionals, and secondly enabled a broad study of distinct permutations and compositions as we will discover in the next chapters. However the application of the special quasi-random structures method to HEAs is not necessarily straightforward. Recalling from section 4.3 the first initial concern is the size of the SQS model and if it's sufficient enough to correctly model the disordered multi-component structure. In this section we will consider this problem by studying the difference between the 48 atom SQS to that of a 96 and 192 atom SQS with volume 1200Å³ and 2400 Å³ respectively. The computational demand for the 3 sizes is seen below in figure 7.11 where we plot the number of CPU hours as a function of number of atoms.

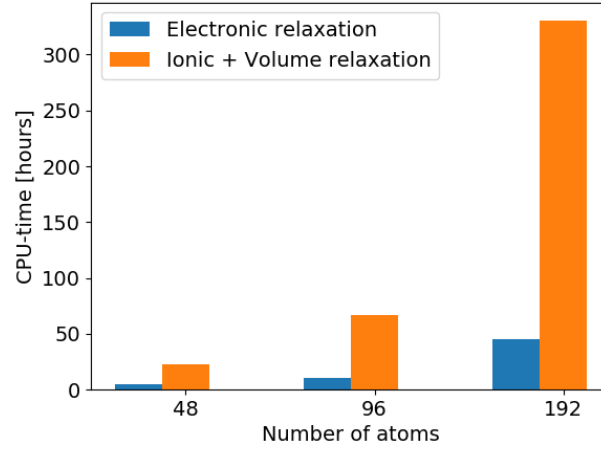


Figure 7.11: CPU time

Bellow we list the mean and standard deviation of the total energy, magnetic moment and enthalpy of formation of the 3 sizes in table 7.6, and band gaps in table 7.7.

SQS size	Toten (eV)		Mag (μ_B)		E_{FPA} (eV)
	mean	std	mean	std	mean
48 atoms	- 6.6105	..	0.0833	0.0000	-0.292
96 atoms	- 6.6092	0.0021	0.0708	0.0114	-0.292
192 atoms	- 6.6123	0.0022	0.0761	0.0171	-0.295

Table 7.7: Total energy, magnetic moment and formation energy of 48, 96 and 192 atom SQSs of (CrFeMnNi)Si₂

As seen from table 7.4 the total energy, magnetism and corresponding

formation energy show very minimal variation. Moreover we find no clear trend of convergence with increasing SQS size contrary to the discussion in section 3.3, however we have only conducted a search over 3 sizes with large difference and based on the mean energy of 5 structures, hence these results could be different in a broader study. But based on our results we find good indication of that the 48 atom model adequately describe the compound. The band gaps listed in table 7.8 is first of all evident across all 3 SQS models and show similar polarization favoring the spin up direction. In several cases, we find that increasing the SQS size reduce the magnitude of the band gaps.

SQS size	SQS	$E_G^{up,eigen}(0.5)$ (eV)	$E_G^{dw,eigen}(0.5)$ (eV)	$E_G^{tot,eigen}(0.5)$ (eV)
48 atoms	A	0.0815	0.0521	0.0281
	B	0.2932	0.0523	0.0523
	C	0.2355	0.0343	0.0343
	D	0.3386	0	0
	E	0.3078	0.0495	0.0495
96 atoms	A	0.1705	0.0442	0.0367
	B	0.1386	0.0270	0.0270
	C	0.1347	0.0363	0.0075
	D	0.0892	0.0398	0.0398
	E	0.1610	0	0
192 atoms	A	0.1197	0.0321	0.0321
	B	0.1444	0	0
	C	0.1867	0	0
	D	0.0478	0.0339	0
	E	0.0131	0.0184	0.0131

Table 7.8: Band gap of SQSs of 48, 96 and 192 atoms each of (CrFeMnNi)Si₂. The names are arbitrary, ie A in 48 does not equal A in 96 or 192.

Similar to structure D in the 48 atom SQS we find that the 0 value in SQS E in the 48 atom model suffers from defect states and find $E_G^{dw,eigen}(0.90,0.10) = 0.016$ eV. The same is true for SQS B and C (192), but require $occ = 0.999, 0.001$ to locate a small nonzero spin down band gap. The band gap in SQS D and E (192) on the other hand is finite at $occ = 0.5$ but can be enlarged from increasing occ . In D we get $E_G^{up,eigen}(0.99) = 0.075$ eV and $E_G^{dw,eigen}(0.01) = 0.05$ eV and similarly $E_G^{up,eigen}(0.99) = 0.05$ eV, and $E_G^{dw,eigen}(0.01) = 0.048$ eV in E. In such cases where the eigenvalues inclusive of defect states return a finite band gap, the density of states does not. This is seen in figure 7.12 for SQS E in the 192 atom SQS.

Drawing any conclusion on the band gaps is difficult seeing as we find very different results within all 3 sizes. Based solely on the most stable SQS it's clear that the larger cell produce a much lower and different band

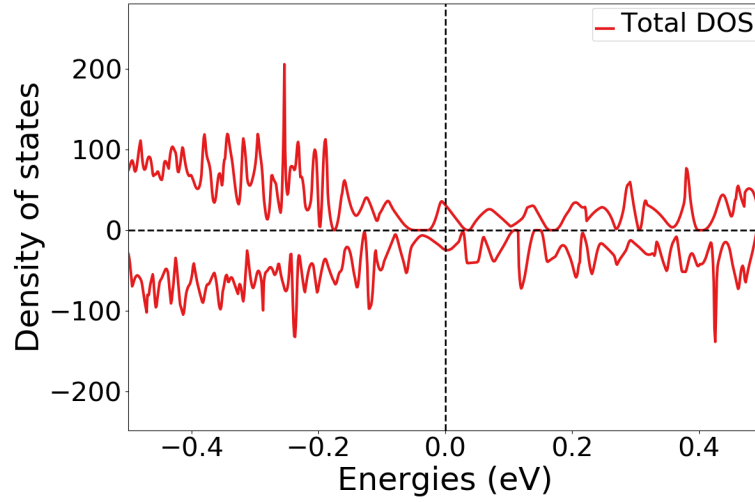


Figure 7.12: Density of states of SQS E 192 atom SQS.

gaps compared to the moderate SQS sizes which are much more similar. However also here we find that the gap in the 96 cell is only about half of the 48 atom cell. However as seen in table 7.7 we also find evidence of large band gaps in the larger cells in other atomic configurations. This goes back to section 3.3 where we mentioned that one of the biggest drawbacks of the special quasi-random structures method is the large number of possible atomic configurations, thus in order to conclude between results in this project the most sensible point is to consider the most stable SQS, but as seen from the very varying properties between SQSs of the same model, this does not necessarily been the most stable SQS if we trialed 20 SQSs instead of just 5. On the other hand, based on this narrow search it appears that the band gap is less frequent and smaller as we increase the size of the SQS model.

Looking at the pair distribution functions in figure 7.13 we see that the local ordering and short-range interactions is well represented and identical across all three sizes. The distinctions of preferences could as stated above simply be a product of the uniqueness of the SQSs more so than the size. On the other hand the larger SQSs clearly provide a better description of large-range interactions, that is not nearly as present in the smaller cell. However as seen in table 7.4 and in accordance with the fundamental concept of the special quasi-random structures method is that the functional properties is mostly determined by short-range effects in the lattice. However there is a possibility that the long range interaction have an affect on the listed band gaps. As disucssed in section 4.3, one of the drawbacks of DFT is modeling of weak long-range interactions, thus this could play a role in the results. In general despite the fact that the larger SQSs is clearly more adapt to model the disordered structure, the improvement is not justified from the cost, as illustrated in figure 7.11. And the apparent larger concern of the SQS method in this project is the uniqueness of each SQS.

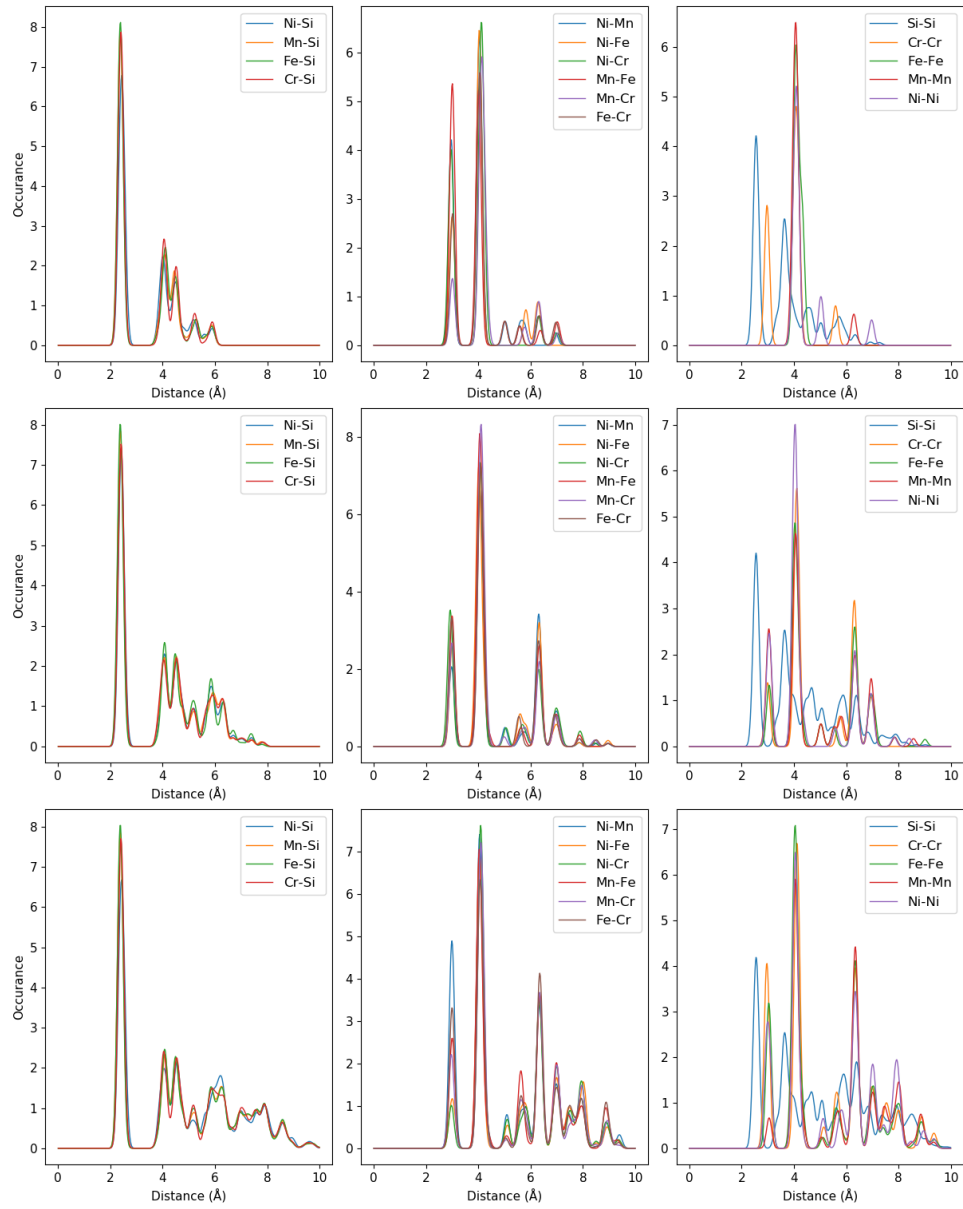


Figure 7.13: Pair distribution functions of SQS sizes (top) 48 atoms, (middle) 96 atoms, (bottom) 192 atoms

Chapter 8

Other compositions

Up until this point we have looked in detail at the high-entropy silicide (CrFeMnNi)Si₂ and associated SQSs. However these structures are just the center of a quaternary phase diagram consisting of the different possible distributions of elements. Thus there exists many other possible compositions related to the previously explored (CrFeMnNi)Si₂ high-entropy silicide. In the two following sections we will analyze some of the different possibilities, starting with a discussion on alloys based on the same elements but with different distributions. Thereafter we will look at alloys where chromium, manganese or nickel are replaced with cobalt or titanium.

8.1 Exploring the quaternary phase-diagram

In this section, we aim to expand our search of this diagram by generating SQSs of the 48 atom model slightly away from equimolar distribution of 3d elements. In table (bellow) we list the mean total energy and magnetic moment per atom with standard deviation and the enthalpy of formation of 4 compositions of the (CrFeMnNi)Si₂ alloy. Ideally they would differ only by one element, but the TDEP implementation insist in also reducing Nickel to stay consistent with the 48 atom supercell, therefore we include a composition with solely larger amounts of nickel as well.

Composition	Toten (eV)		Mag (μ_B)		E_{FPA} (eV)
	mean	std	mean	std	mean
Cr ₃ Fe ₃ Mn ₇ Ni ₃ Si ₃₂	- 6.6947	0.0040	0.1375	0.0186	-0.300
Cr ₅ Fe ₅ Mn ₃ Ni ₃ Si ₃₂	- 6.6705	0.0030	0.1127	0.0223	-0.286
Cr ₅ Fe ₃ Mn ₅ Ni ₃ Si ₃₂	- 6.6852	0.0041	0.1375	0.0456	-0.271
Cr ₃ Fe ₅ Mn ₅ Ni ₃ Si ₃₂	- 6.6801	0.0036	0.0937	0.0209	-0.315
Cr ₃ Fe ₃ Mn ₃ Ni ₇ Si ₃₂	- 6.3921	0.0078	0.0159	0.0101	-0.285

Table 8.1: Summary composition diagram

In table 8.1 we observe that moving away from the equimolar system generally result in lesser stable compositions, with the immense exception of compositions rich in nickel. Here we find that the formation energy is about twice the amount of the other compositions and additionally exceeds the equimolar system. The physical reason behind why nickel have such a large effect on the enthalpy of formation is beyond the scope of this study, but we do note that we have not found any indication of nickel stabilizing high-entropy alloys or silicides, but in terms of mathematics it's sensible that δH is larger from the low total energy of nickel (5.58eV) compared to for example Cr (9.51eV) or Mn (9.03).

Compared to the equimolar system, the magnetic moment of these compositions show a greater variation between SQSs, as indicated by the standard deviation. Typically the most stable SQS lie around the mean value of the set. The large magnetic moment of the manganese rich permutation and the low magnetic moment in the chromium poor permutation is very much in line with the observations made in the previous section. Recalling that in the magnetic moment in the equimolar composition was largely attributed to manganese and chromium atoms in the lattice. Thus increments to manganese or reduction of chromium would following impact the magnetic moment as seen. Following the composition $\text{Cr}_5\text{Fe}_3\text{Mn}_5\text{Ni}_3\text{Si}_{32}$ where the nonmagnetic elements are reduced and the magnetic elements are increased, the final magnetic moment is among the highest of the bunch equally magnetic.

In table 8.2 we list the respective band gaps of the different compositions calculated with the PBE functional. Only the GGA functional was applied in this case because the motivation is primarily to compare the results to the parent equimolar composition and thus including 3 times as many results to calculate and analyze unnecessarily complicate the process. Thus we base this comparison between the PBE results of the new compositions to the PBE band gaps of the equimolar compound. In these compositions we find strong indication of a half-metal with less frequent SQSs with a band gap in the spin down channel than the equimolar compound. In the spin up channel on the other hand several compositions show very similar values to the equimolar composition. Between the different compositions particularly those rich in manganese provide very encouraging results and compositions poor in Mn less so. In terms of the stability we a very encouraging results of both the $\text{Cr}_3\text{Fe}_3\text{Mn}_7\text{Ni}_3\text{Si}_{32}$ and $\text{Cr}_3\text{Fe}_5\text{Mn}_5\text{Ni}_3\text{Si}_{32}$ compositions, where the most promising properties is attributed to the utmost stable configurations. in $\text{Cr}_3\text{Fe}_5\text{Mn}_5\text{Ni}_3\text{Si}_{32}$ the most stable SQS (D) is a semiconductor with a band gap around 0.1 eV .

Composition	SQS	$E_G^{\text{up, eigen}}(0.5)$ (eV)	$E_G^{\text{dw, eigen}}(0.5)$ (eV)	$E_G^{\text{tot, eigen}}(0.5, 0.5)$ (eV)
$\text{Cr}_3\text{Fe}_3\text{Mn}_7\text{Ni}_3\text{Si}_{32}$	A	0.3390	0	0
	B	0.4745	0	0
	C	0.1342	0	0
	D	0.1950	0.0063	0.0063
	E	0.4211	0	0
$\text{Cr}_5\text{Fe}_5\text{Mn}_3\text{Ni}_3\text{Si}_{32}$	A	<i>0.003</i>	0	0
	C	<i>0.21</i>	0	0
	D	0.0674	0.0413	0.0372
	E	<i>0.362</i>	0	0
$\text{Cr}_5\text{Fe}_3\text{Mn}_5\text{Ni}_3\text{Si}_{32}$	A	0.2082	0	0
	B	0.4053	0	0
	C	0.4659	0	0
	D	0.0843	0.0121	0.0121
	E	0.3008	0	0
$\text{Cr}_3\text{Fe}_5\text{Mn}_5\text{Ni}_3\text{Si}_{32}$	A	0.3922	0	0
	C	0.1285	0	0
	D	0.2595	0.1004	0.1004
	E	0.3591	0.1003	0.0848
$\text{Cr}_3\text{Fe}_3\text{Mn}_3\text{Ni}_7\text{Si}_{32}$	A	0	0	0
	B	0	0	0
	C	0	0	0
	D	0	0	0
	E	<i>0.04</i>	0	0

Table 8.2: Band gaps of various compositions of $(\text{CrFeMnNi})\text{Si}_2$. Most stable SQS of a set is highlighted in bold text, defect band gap are listed in cursive. Some SQSs were excluded from the table due to unsuccessful calculations.

Below in figure 8.1 we plot the projected density of states around E_F of the first four compositions of table 8.2. Note that away from the Fermi energy the projected density of states is analogous to the parent equimolar composition. The below figures is based on the most stable SQS in each permutation, as will the analysis. Hence the features of these figures can be subject to the uniqueness of that particular SQS rather than a distinct feature of the exact composition, but as stated previously the most stable configuration provide the most likely properties of the composition within the scope of this project.

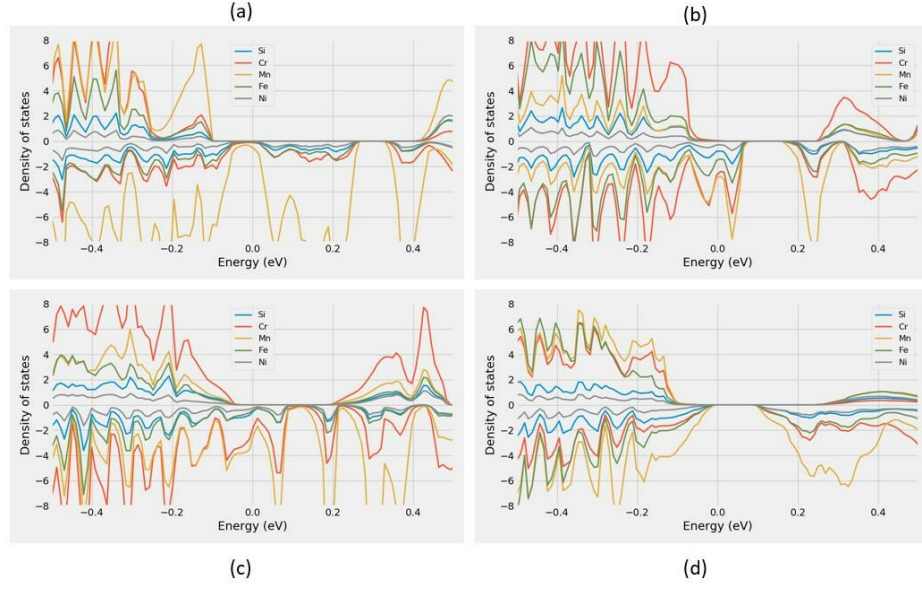


Figure 8.1: Projected density of states of (a) $\text{Cr}_3\text{Fe}_3\text{Mn}_7\text{Ni}_3\text{Si}_{32}$ (SQS B), (b) $\text{Cr}_5\text{Fe}_5\text{Mn}_3\text{Ni}_3\text{Si}_{32}$ (SQS C), (c) $\text{Cr}_5\text{Fe}_3\text{Mn}_5\text{Ni}_3\text{Si}_{32}$ (SQS A), (d) $\text{Cr}_3\text{Fe}_5\text{Mn}_5\text{Ni}_3\text{Si}_{32}$ (SQS D)

With that said, the plotted PDOSs in figure 7.1 is in good agreement with the listed values in table 7.2. $\text{Cr}_3\text{Fe}_3\text{Mn}_7\text{Ni}_3\text{Si}_{32}$ (7.1 a) and $\text{Cr}_5\text{Fe}_3\text{Mn}_5\text{Ni}_3\text{Si}_{32}$ (7.1 c) both indicate a sizable spin up band gap, further figure (7.1 d) point to a total band gap around 0.1 eV for SQS D of $\text{Cr}_3\text{Fe}_5\text{Mn}_5\text{Ni}_3\text{Si}_{32}$. On the other hand we find dissimilarity between the density of $\text{Cr}_5\text{Fe}_5\text{Mn}_3\text{Ni}_3\text{Si}_{32}$ SQS C and the eigenvalue band gap listed in table 7.2. In figure 7.1 d we find a range of forbidden energies slightly above the Fermi energy, and very small values in spin up at the Fermi energy. Similar to what we experienced in the 192 atom SQS in section 7.4, the eigenvalues report a finite band despite of defect states. Therefore the density of states is not completely zero at E_F .

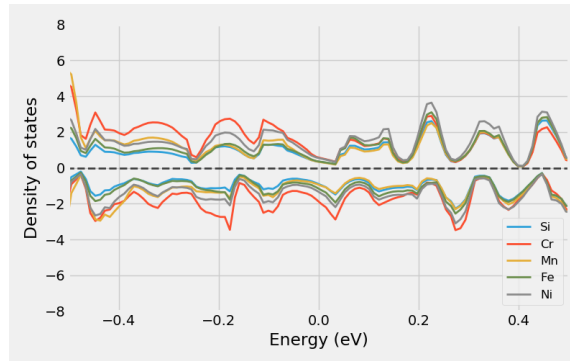


Figure 8.2: Projected density of states of $\text{Cr}_3\text{Fe}_3\text{Mn}_3\text{Ni}_7\text{Si}_{32}$ around E_F

In figure 8.6 we saw that electrons from manganese atoms in particular was a key contributor as to why the spin down channel of $(\text{CrFeMnNi})\text{Si}_2$

was metallic in the stable supercell D. This is also largely the case in the permutations shown above in figure 8.12. The proportion of manganese atoms in the alloy seems to offer a very positive effect on the band gap in spin up, but is often detrimental to spin down. This is seen in figure 8.12 (a) and (c) for $\text{Cr}_3\text{Fe}_3\text{Mn}_7\text{Ni}_3\text{Si}_{32}$ and $\text{Cr}_5\text{Fe}_3\text{Mn}_5\text{Ni}_3\text{Si}_{32}$ respectively, that both contain increased amounts of manganese. By reducing the number of Mn as in (b) we still find that the Mn electrons plague the states at E_F in spin down. In analog we see from (b) and (c) that also Cr negatively impacts to the band gap especially in spin up. The sole permutation with clear evidence of a spin down gap is from the chromium poor permutation plotted in (d). Also in this structure we see that the effects of Mn around E_F is dampened in comparison to the other permutations, despite containing relatively increased amounts of Mn to the eqvimolar alloy.

An important property of these results is that because each composition alters simultaneous elements, interpreting and relating the results to a particular alteration is challenging. For example, is the result of the $\text{Cr}_5\text{Fe}_3\text{Mn}_5\text{Ni}_3\text{Si}_{32}$ permutation a consequence of less Fe or increments to both Cr and Mn? Furthermore is the large band gap in spin up of $\text{Cr}_3\text{Fe}_3\text{Mn}_7\text{Ni}_3\text{Si}_{32}$ a product of increasing manganese or reducing the other elements. From the comparatively large gaps in spin up of $\text{Cr}_3\text{Fe}_3\text{Mn}_7\text{Ni}_3\text{Si}_{32}$ and $\text{Cr}_3\text{Fe}_5\text{Mn}_5\text{Ni}_3\text{Si}_{32}$ and the more present Cr states in spin up in the Cr rich permutations we here conclude that the band gap is related to lessening of chromium, more so than other effects. However we see from both $\text{Cr}_5\text{Fe}_5\text{Mn}_4\text{Ni}_3\text{Si}_{32}$ and $\text{Cr}_3\text{Fe}_3\text{Mn}_3\text{Ni}_7\text{Si}_{32}$ (figure 8.2) in addition to the manganese rich composition that Mn plays a vital role on the band gap of these structures. It's clear that the $\text{Cr}_3\text{Fe}_5\text{Mn}_5\text{Ni}_3\text{Si}_{32}$ alloy manage to strike a balance between 3d elements that results in a specific interplay and correspondingly very promising properties. In addition we see from the enthalpy of formation that the compositions poor in chromium are more stable than the chromium rich compositions.

8.2 High entropy silicides with cobalt and titanium

In similar fashion to the previous sections, we here begin by presenting the mean and standard deviation of the total energy and magnetization of a set of SQSs corresponding to different high-entropy silicides of the FeSi_2 unit cell. The compositions we have tested are deliberate combinations intended to investigate both the impact of manganese by replacing the element with Co or Ti, and concepts related to HEA theory such as the atomic size effect. Furthermore Co is a very common element in many stable HEA, as seen in section 2.2, thus we include 3 compositions with Co to study the impact on stability and the functional properties. The results of the aforementioned alloys can be seen below in table 9.1, note that all compounds contain a total of 48 atoms as before.

Composition	Toten (eV)		Mag (μ_B)		E_{FPA} (eV)
	mean	std	mean	std	mean
$\text{Cr}_4\text{Fe}_4\text{Co}_4\text{Ni}_4\text{Si}_{32}$	-6.4655	0.0056	0.0083	0.0155	-0.308
$\text{Co}_4\text{Fe}_4\text{Mn}_4\text{Ni}_4\text{Si}_{32}$	-6.4731	0.0046	0.0000	0.0000	-0.355
$\text{Cr}_4\text{Fe}_4\text{Ti}_4\text{Ni}_4\text{Si}_{32}$	-6.4217	0.0087	0.0305	0.0293	-0.209
$\text{Cr}_4\text{Fe}_4\text{Mn}_4\text{Ti}_4\text{Si}_{32}$	-6.6994	0.0071	0.1142	0.0641	-0.199
$\text{Cr}_4\text{Fe}_4\text{Mn}_4\text{Co}_4\text{Si}_{32}$	-6.7687	0.0034	0.1331	0.0326	-0.323

Table 8.3: Overview new compositions

From table 9.1 we see that the stability of the relative compositions vary greatly. By introducing cobalt to the alloys, particularly at the cost of chromium result in a large positive effect on the stability, contrary replacing either manganese or nickel with titanium significantly lowers the stability. A physical interpretation of the relative stability is difficult from the overall shallow emphasis and analysis in this project, but we do note that the two most stable alloys consist of the most chemically similar elements in terms of properties such as electronegativity and atomic size. Following the least stable alloys according to our study is comprised of the most chemically dissimilar elements. This is in good agreement with our discussion in section 2.2 regarding phase formation of high-entropy alloys.

In table 9.1 we have listed the mean magnetic moment of the compositions, in line with previous results in this project the magnetization is very dependent on chromium and manganese. This is seen by the overall lowest magnetic moments in the two compositions without these elements, and reversely the highest magnetic moments is found for compositions with both Cr and Mn. Comparing the magnetic moment of $(\text{CrFeCoNi})\text{Si}_2$ and $(\text{CoFeMnNi})\text{Si}_2$ it seems in our study that chromium is most responsible for the magnetic moment in these alloys. Furthermore we find that substituting Ni with both Ti and Co result in more magnetic compounds. These are truly surprising results, one would expect that the magnetic moments would be larger in the ferromagnetic elements Ni, Fe and Co than Cr, Mn and Ti. This could go back to our simplistic and superficial study of the magnetic properties in this project, additionally the PBE functional as we covered in section .. have shown limitations for 3d elements and particularly Ni. Thus this could be a factor affecting our results. Another factor is that we here based our comparison on the mean values between 5 SQSs. As we have experienced throughout this project the uniqueness of the SQSs can be troublesome to handle, and our best guess is to study the most stable super-cell. Below in table 9.2 we list the magnetic moments of the most stable SQSs. Here we find several dissimilarities to the mean value such as the $\text{Cr}_4\text{Fe}_4\text{Co}_4\text{Ni}_4\text{Si}_{32}$ being nonmagnetic in the most stable supercell. Thus based on the utmost stable configurations we can state that replacing either Cr or Mn (with Co) removes the magnetic moment in the alloy. Furthermore we find from these supercells that the magnetic moment is reduced

by replacing Ni with Ti, and increased from Co. These results are in much better accordance with previous knowledge of ferromagnetic elements and their interplay in high-entropy alloys.

Composition	Magnetic moment (μ_B)
$\text{Cr}_4\text{Fe}_4\text{Co}_4\text{Ni}_4\text{Si}_{32}$	0
$\text{Co}_4\text{Fe}_4\text{Mn}_4\text{Ni}_4\text{Si}_{32}$	0
$\text{Cr}_4\text{Fe}_4\text{Ti}_4\text{Ni}_4\text{Si}_{32}$	0,0653
$\text{Cr}_4\text{Fe}_4\text{Mn}_4\text{Ti}_4\text{Si}_{32}$	0,0785
$\text{Cr}_4\text{Fe}_4\text{Mn}_4\text{Co}_4\text{Si}_{32}$	0,1666

Table 8.4: Final magnetic moment of the most stable supercell of each composition.

In regards to the band gap of these compositions, we find most to be metals. The band gap of the most stable SQS of each composition is listed in table 4.3, where we calculate the band gap from the eigenvalues at different occupancy cutoffs. As before the 0 band-gap is caused by defect states in the band gap. By increasing the criteria, in other words only consider states with occupancy above a certain threshold, the band gap become finite at $occ = 0.1$ and converge to around 0.02 – 0.06 eV depending on composition, when only considering full/empty states.

Composition	occ	$E_G^{\text{up, eigen}}$ (eV)	$E_G^{\text{dw, eigen}}$ (eV)	$E_G^{\text{tot, eigen}}$ (eV)
CrFeCoNiSi_2	0.5	0	0	0
	0.1	0.00095	0.0399	0.00095
	0.01	0.063	0.063	0.063
CrFeTiNiSi_2	0.5	0.0067	0	0
	0.1	0.061	0.0087	0.0087
	0.01	0.061	0.037	0.037
CoFeMnNiSi_2	0.5	0	0	0
	0.1	0.0037	0.0037	0.0037
	0.01	0.0268	0.0268	0.0268
CrFeMnTiSi_2	0.5	0	0	0
	0.1	0.021	0.00049	0
	0.01	0.03	0.03	0.022
CrFeMnCoSi_2	0.5	0.461	0	0
	0.1	0.607	0.0218	0.0218
	0.01	0.607	0.0245	0.0245

Table 8.5: Band gaps of the most stable SQS of β -FeSi₂ high-entropy silicide compositions as a function of occupancy in the eigenvalues.

In the CrFeMnCoSi_2 composition we observe a band gap of around 0.5 eV in the spin up channel, contrary to the metallic or very narrow band gaps in the other compositions. But also in this case we find that the eigenvalues contain defect states, by the fact that the band gap can be enlarged at lower values of occ . As we have covered for other examples in this project, this results in a metallic density of states with a small number of states at the Fermi energy. This can be seen from the projected density of states in figure 8.3. This is a contradicting result to the eigenvalues, as per the definition, a band gap is defined as a range of energies around E_F with no states. On the other hand, this result could rather be related to numerical factors affecting the accuracy of the density of states, such as a low resolution or number of k-points considering the very marginal difference separating the density of states from a metal to a half-metal.

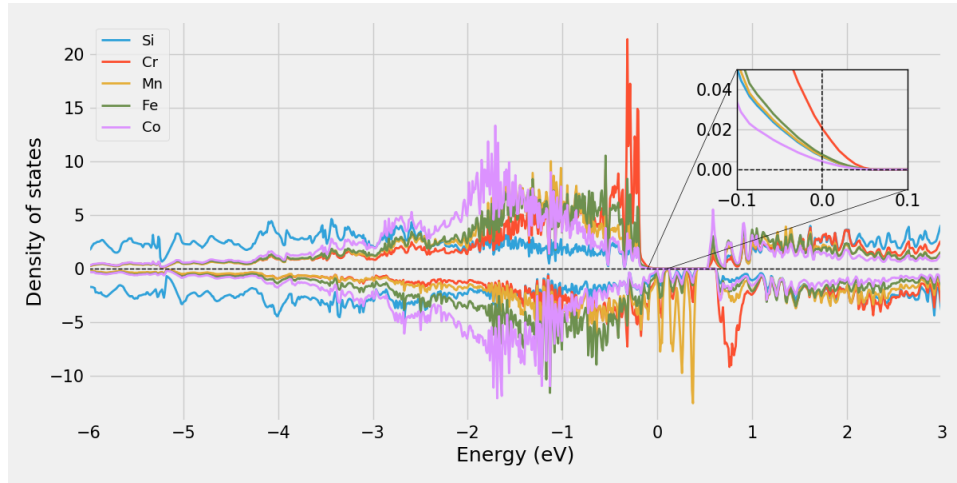


Figure 8.3: Projected density of states of $(\text{CrFeMnCo})\text{Si}_2$.

The concept of defect states remain as the unsolved biproduct of this project, that we have seen is clearly related to a metallic structure, but is less prominent in the alloys. However considering the scope and allocated time/resources of this project we have not been able to investigate this concept further and found minimal literature to base our results and discussion on. Thus we are unable to provide a conclusion on firstly the significance and physical interpretation of it, and secondly why they appear in some compositions/structures but not others but report that it's less apparent in the $(\text{CrFeMnNi})\text{Si}_2$ system. One possible method of analyzing it could have been to study more in depth the pair distribution functions and compare between all compositions, but given the uniqueness of the SQSs and number of bonds in each structure this falls outside the scope of this project. We report the related PDF's of each composition in appendix .. but do not discuss them. The projected density of states of each composition is found in appendix ..

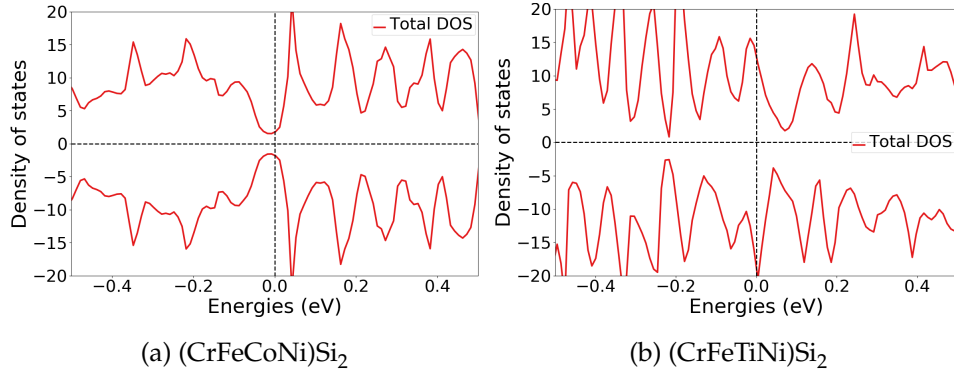


Figure 8.4: Density of states of a) (CrFeCoNi)Si₂ and b) (CrFeTiNi)Si₂.

Contrary to the above case, inserting Co in the place of manganese clearly result in a metallic structure, as seen in the density of states in figure 9.2 a. Replacing Mn with Ti instead we recall from table 9.3 a a very small defect band gap in spin up, however from figure 9.2b we observe that E_G^{dos} is equal to zero, thus again $E_G^{dos} \neq E_G^{eigen}$. Comparing the density of states of (CrFeCoNi)Si₂ and (CrFeTiNi)Si₂ the latter is magnetic and the former nonmagnetic, as we discussed previously.

Above we have looked at the band gap of the most stable SQS of each composition, but as we have experienced in other cases in this project, the properties can vary between SQSs of the same composition. In both CrFeCoNiSi₂ and CrFeMnTiSi₂ we found only metallic supercells with the exception of one SQS in the latter with a very small defect band gap in spin up. Similarly small defect band gaps was observed in two SQSs of CrFeTiNiSi₂ and the rest as metals. In CrFeMnCoSi₂ we found a large defect band gap in spin up in the most stable configuration, here we find similar band gaps in two other SQSs as well. The most interesting case was found in CoFeMnNiSi₂ where we observed small total band gaps without defect states in two SQSs, these are seen in figure 9.3. In agreement with the nonmagnetic character of this composition, the DOS is symmetric with respect to spin.

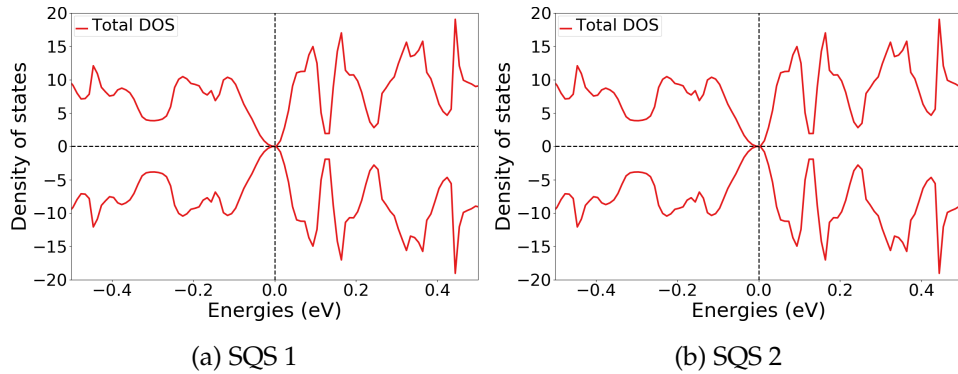


Figure 8.5: Density of states of two lesser stable SQSs of (CoFeMnNi)Si₂.

In this example, and also throughout this project we have experienced

scenarios where the most stable SQS represents the set of supercells well, and in other instances where the properties change from supercell to supercell. Because of the limited efforts on the magnetism and corresponding stability of the alloys in this project, we chose to include and discuss all 5 SQSs in several cases. This goes back to the topics discussed previously in which one might expect the real material to be comprised of domains of local ordering equal to each one of the SQSs and other possible configuration by a probability based on the relative stability. Furthermore we have reservations about the SQS approach in general to produce an accurate depiction of the true disordered structure, particularly at the relative small size. As we experienced in section .., noteworthy the band gap and PDFs showed distinctions between cells, an additional point to this is that the SQS method have prior limitations of compositions with large deviation from the equiatomic composition, compared to methods such as the CPA for instance.

Now that we in this study have quite qualitatively determined the existence of a band gap in a potential high-entropy silicides, and according to our calculations in the $(\text{CrFeMnNi})\text{Si}_2$ composition based on the cmce crystal structure. In future work we would first and foremost do a more comprehensive configuration of the magnetic moments to qualitatively determine the ground state energy and compare the relative stability between a broader number of crystal structures. Going back to section 4.3, one of the key drawbacks of the DFT is that we only find local minima, thus from this project we have no knowledge of this particular composition stabilize in the structure tested in this project or another one. On this topic, recent findings have supported high-entropy silicides stabilizing in less symmetric structures such as orthorhombic and hexagonal **Cite this and that** as opposed to initial studies indicating that HEAs are primarily found in simple cubic lattices. But this should be tested nevertheless. With a more precise conclusion on both geometric and magnetic factors of the material, we could have performed a deeper analysis of the band gap and put more effort into converging calculations without uncertainties of band-gap specialized functionals such as HSE06 and MBJ, and to a greater extent investigated the defect states in the eigenvalues, and relate this qualitatively to a physical or numerical factor.

Following studies on the ground state geometry and energy, the composition should be exposed for finite temperatures to evaluate the magnetism and transition temperatures, and entropic contributions to the stability through Gibbs law, in addition to a number of other considerations. Nevertheless we have succeeded atleast within the scope of this project, in our task of locating high-entropy alloys/silicides with a band gap. Furthermore the magnitude of the band gap in many instances (between 0.01 - 0.1 eV) would make for promising candidate thermoelectric materials. However to qualitatively state the promise of these compositions as thermoelectrics one would have to investigate properties such as the Seebeck coefficient in addition to the electrical and thermal conductivity. But based on the findings of similar materials to the one in this project, such as .. that found lowered thermal conductivity in .. and ,.. in this and

that, the possibility of an effective thermoelectric material is not beyond hope. In addition the strong magnetism and spin polarization of the band gap displayed in this material (according to our narrow study) makes it a promising candidate for spintronics application.

Part IV

Conclusion

Write conclusion here

Bibliography

- [1] S. J. Clark et al. 'Structure and electronic properties of FeSi₂'. In: *Phys. Rev. B* 58 (16 Oct. 1998), pp. 10389–10393. DOI: 10.1103/PhysRevB.58.10389. URL: <https://link.aps.org/doi/10.1103/PhysRevB.58.10389>.
- [2] Voicu Popescu and Alex Zunger. 'Effective Band Structure of Random Alloys'. In: *Phys. Rev. Lett.* 104 (23 June 2010), p. 236403. DOI: 10.1103/PhysRevLett.104.236403. URL: <https://link.aps.org/doi/10.1103/PhysRevLett.104.236403>.
- [3] R. Eppenga. 'Ab initio band-structure calculation of the semiconductor β -FeSi₂'. In: *Journal of Applied Physics* 68.6 (1990), pp. 3027–3029. DOI: 10.1063/1.346415. eprint: <https://doi.org/10.1063/1.346415>. URL: <https://doi.org/10.1063/1.346415>.
- [4] H Lange. 'Electronic properties of semiconducting silicides'. In: *physica status solidi (b)* 201.1 (1997), pp. 3–65.
- [5] Stewart Clark. 'Modelling complex structures'. URL: <http://cmt.dur.ac.uk/sjc/thesis/thesis/node28.html>.
- [6] *ISMEAR - Vaspwiki*. URL: <https://www.vasp.at/wiki/index.php/ISMEAR>.